Size-Dependent Lattice Structure and Confinement Properties in $CsPbI_3$ Perovskite Nanocrystals: Negative Surface Energy for Stabilization

Authors: Qian Zhao,[1,2,3] Abhijit Hazarika,[2] Laura T. Schelhas,[4] Jun Liu,[2] E. Ashley Gaulding,[2] Guoran Li,[3] Minghui Zhang,[1] Michael F. Toney,[4] Peter C. Sercel,[5] Joseph M. Luther[2]*

Affiliations:

[1]College of Chemistry, Nankai University, Tianjin 300071, China

[2]National Renewable Energy Laboratory, Golden, CO 80401, USA

[3]Institute of New Energy Material Chemistry, Nankai University, Tianjin 300350, China

[4]SLAC National Accelerator Laboratory, Menlo Park, CA 94025, USA

[5]T. J. Watson Laboratory of Applied Physics, California Institute of Technology, Pasadena, CA 91125, USA

*Correspondence to: joey.luther@nrel.gov

Abstract:

$CsPbI_3$ colloidal nanocrystals with narrow size distributions were prepared with average sizes ranging from 5 to 15 nm to study the size dependent properties of the metal halide perovskite material. Structurally, the nanocrystals adopt the perovskite structure (over the non-perovskite orthorhombic structure) with much greater stability than thin film and bulk materials of the same composition. Among the potential perovskite phases (cubic α, tetragonal β, and orthorhombic γ), we find samples are best characterized by the γ phase, rather than the often reported α phase, but may have a size dependent average tilting between adjacent lead iodide octahedra. Specifically, we find size-dependent lattice constants systematically varying by 3% across the size range, with unit cell volume expansion increasing linearly with the inverse of nanocrystal size to 2.1% for the smallest size nanocrystals. We estimate the negative surface energy to be between -3.0 and -5.1 eV nm^{-2} for these oleate and oleylammonium capped $CsPbI_3$ colloidal nanocrystals. Moreover, the nanocrystal size-dependent bandgap is analysed and is found to be best described using an intermediate confinement model. This model more accurately describes size dependent properties in all-inorganic perovskites than previous work and is the first model reported specifically for $CsPbI_3$. We experimentally determine the bulk band gap energy, effective mass and exciton binding energy, concluding with variations from the bulk α-phase values. This provides a robust route to understanding more about the γ-phase properties of $CsPbI_3$.

Introduction

In the last decade, tremendous headway has been made toward the application of metal halide perovskite (MHP) semiconductors as either absorber materials for photovoltaics, detectors, scintillators or as light emitters for displays, LEDs, lasers, etc.[1–6] A solid grasp of the fundamental

Pursuant to the DOE Public Access Plan, this document represents the authors' peer-reviewed, accepted manuscript. The published version of the article is available from the relevant publisher.

material properties is thus certainly warranted. The quantum confinement properties enabled by colloidal nanocrystal (NC) synthesis not only offers the opportunity to tune light emission wavelength but can also be used to understand basic properties and determine material parameters, such as the bulk bandgap value, Bohr radius and binding energy of excitons, effective masses, etc. There is an open opportunity in colloidal perovskite NCs to better understand the effects of size such as the size dependent absorption and emission properties due to quantum confinement, and size dependent strain, lattice, and structural properties. Not only from the fundamental properties point of view but determining the crystal lattice properties like distortions has also direct implications on electric polarizability, large polaron formation, and ferroelectric behavior of MHPs that may lead to new devices or phenomena.[7–11] In this work, we specifically study $CsPbI_3$ NCs widely used in high efficiency colloidal quantum dot solar cells, LEDs, and photodetectors.[12–18]

Interestingly, the "softness" of the lattice is a key characteristic which sets these crystalline MHP materials apart from traditional inorganic semiconductors. The elastic softness makes MHPs more prone to strain and strain-related effects as well as lattice dynamic effects.[19–24] It has been noted that certain phases may emerge as a average of the dynamical crystal.[25] Such dynamical processes promote the ability to use MHPs to develop new technologies that takes advantage of effects like electrostriction or photostriction, switchable ferroelectricity or phase, for example.[26–28]

Studies focusing on the size dependent properties of some MHP NC systems are missing from the literature perhaps due to the difficulty of producing well controlled monodisperse particles over a wide range of sizes. The main challenge in the synthesis of $CsPbX_3$, in general, is the rapid consumption of precursors during hot injection syntheses leading to poor control over nucleation and growth.[29,30] Typical size dispersion of CdSe or PbS quantum dots (QDs) has been reduced to nearly 3% after decades of research, however for MHP NCs, the size dispersion is typically >10%.[31,32] Although the syntheses for MHP NCs like $CsPbBr_3$, $CsPbCl_3$ and $CH_3NH_3PbBr_3$ possessing different morphologies or sizes has been reported,[33–35] appropriate and versatile synthetic preparations for $CsPbI_3$ NCs with independent control of nucleation and growth have not yet been established. To overcome this challenge and generate NCs of appropriate quality for analysis, we have adopted a route using size selective precipitation[36,37] to divide several reactions into batches with relatively tight size distributions among the narrowest reported thus far for $CsPbI_3$. This enables studies of size dependent material properties, which we report here.

Pursuant to the DOE Public Access Plan, this document represents the authors' peer-reviewed, accepted manuscript.
The published version of the article is available from the relevant publisher.

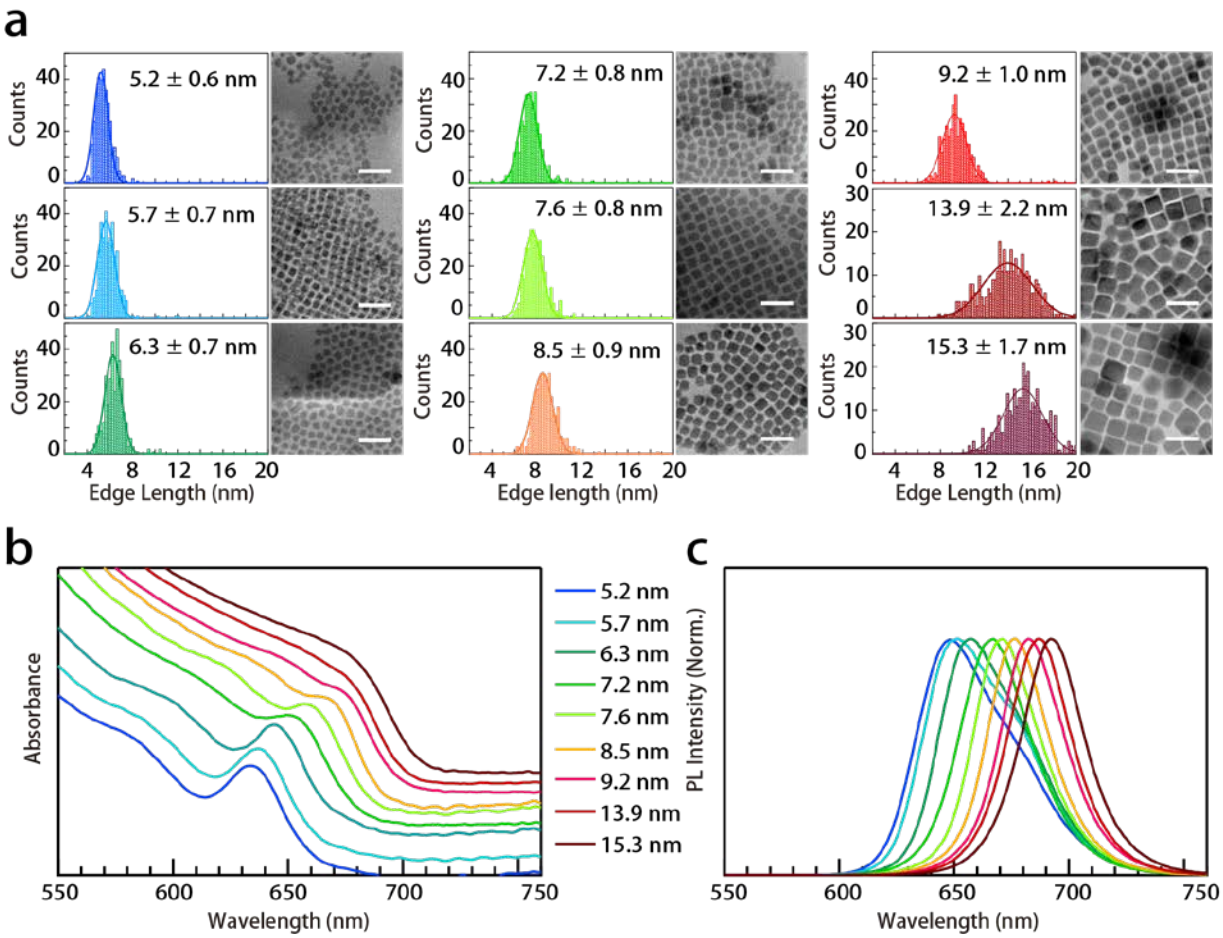

Figure 1. (a) Size distribution histograms (left) and the corresponding TEM images (right) of $CsPbI_3$ NCs with mean size, *L*, of 5.2, 5.7, 6.3, 7.2, 7.6, 8.5, 9.2, 13.9 and 15.3 nm. Here, *L* is the edge length of the NC, assuming the NCs are cube-shaped. The corresponding size dispersions (standard deviation) are 11.5, 12.3, 11.1, 11.1, 10.5, 10.6, 10.8, 15.8 and 11.1%, respectively. Scale bars in all images are 30 nm. (b and c) Optical absorption spectra normalized to their first excitonic peak (offset for clarity) (b) and normalized photoluminescence spectra (c) of $CsPbI_3$ QDs with different sizes, respectively.

In brief, $CsPbI_3$ NCs were synthesized by injection of Cs-oleate into a hot PbI_2 solution containing oleylamine and oleic acid in 1-octadecene held at temperatures ranging between 140 and 185 °C. The QDs were first purified via centrifugation with methyl acetate (MeOAc) and redispersed in hexane. Subsequently the sample size distribution was improved by repeated size-selective precipitations. More details on the synthesis and purification procedures are provided in the methods section.

To explore the achievable size dispersion of $CsPbI_3$ QDs with this method, we analyzed

Pursuant to the DOE Public Access Plan, this document represents the authors' peer-reviewed, accepted manuscript.
The published version of the article is available from the relevant publisher.

TEM images of each aliquot obtained from the various syntheses and size selective precipitations. The distribution of edge lengths, L, for each sample of QDs are shown in Figure 1a. The histograms are determined by analysis of 200 NCs for each sample. The data are binned, plotted, and fitted using a Gaussian to determine the mean size and QD size dispersion. The detailed parameters are shown in Table S1 and the size dispersion is calculated[38] using Eq.1.

$$Size\ dispersion = \frac{Standard\ deviation}{Mean\ size} \times 100\% \quad (1)$$

The size of $CsPbI_3$ QDs using this size-selective method can be tuned from 5.2 ± 0.6 to 15.3 ± 1.7 nm by changing the injection temperatures during syntheses for crude control and optimizing size selective precipitation for fine control. Although adding additives into the reactants to control the size has been reported for $CsPbBr_3$,[39,40] we found this to be more challenging for $CsPbI_3$.

Due to quantum confinement of the electron and hole, the excitonic (and photoluminescence) peak of the $CsPbI_3$ QDs shifted from 678 (692) to 634 (648) nm (Figure 1a–b) as the QD size is reduced from 15.3 to 5.2 nm. We note that in QD samples with average size less than 7 nm, a shoulder is observed to the red of the peak luminescence. This is likely due to a small fraction of larger NCs not all being completely removed via the size selective precipitation. However, these are not seen in sufficient quantity in TEM (Figure 1a). Comparing the low-magnification TEM images and FWHM from photoluminescence (PL) spectra before and after size-selective precipitation (Figure S1), a significant improvement in the uniformity and a reduction in the size distribution are seen. We also compare the PL FWHM of these obtained perovskite QDs with that reported in other works (Table S2), which demonstrates the size distribution in this wide size range is generally the smallest for $CsPbI_3$ QDs although not as narrow as for $CsPbBr_3$ QDs at the present time. Interestingly, with this system we do not observe a size dependent Stokes shift as has been shown and described for $CsPbBr_3$.[41,42] The size independent Stokes shift is 28-49 meV for all samples and is tabulated in Table S1.

In addition to the optical properties, we explore the size dependent structural properties (including lattice constants) and the observed phase. In particular, we comment on the lattice distortions associated with the degree of octahedral tilting to understand the amount of strain present on $CsPbI_3$ QDs. In addition to the size dependent lattice constants, we also explore the crystal structure of the perovskite NCs and examine suggestions that $CsPbI_3$ QDs are described as the α (cubic) phase in various reports since the α phase emerges for high temperature $CsPbI_3$ thin

Pursuant to the DOE Public Access Plan, this document represents the authors' peer-reviewed, accepted manuscript.
The published version of the article is available from the relevant publisher.

films, or as a time average of octahedral tilting in some hybrid perovskites and in oxide perovskites such as $CaMnO_3$.[25,26,43]

As mentioned, one of the more intriguing features found in perovskite NCs is modification of the phase diagram compared to bulk or thin film compositions. This is most notable in the case of $CsPbI_3$. This particular composition is highly desired for photovoltaics. One reason is that $CsPbI_3$ can withstand temperatures of over 460 °C,[44,45] whereas so far, all hybrid materials containing methylammonium or formamidinium suffer from pyrolysis of the organic component over 300 °C.[46,47] This high thermal stability, which is absent in hybrid lead halide perovskite materials, can be useful for subsequent processing involving high temperature or any other high temperature operations. On the other hand, the all-inorganic perovskites also have slightly wider bandgap energies ideal for top cell in multijunction solar cell applications. The largest challenge with $CsPbI_3$ is that the Cs^+ ion is generally too small to retain the corner sharing octahedral geometry required for the perovskite phases, so at temperatures below 330 °C, it is prone to transformation into the non-perovskite orthorhombic δ_{ortho} phase.[48] However, at the nanoscale, it has been shown that the NCs stabilize in a perovksite structure.[13,29] It is believed that the surface-to-volume ratio is so high that surface tension can cause enough tensile strain for the crystal to remain in the perovskite structure at room temperature.[13] Various approaches have been demonstrated to apply tensile strain to thin films of $CsPbI_3$ including lattice anchoring[24] by forming epitaxial heterointerfaces with materials with slightly larger lattice constant or substrate clamping which involves mechanically stretching a film to impart the strain.[22] Negative surface tension has been found in certain nanoparticle systems such as Ni[49], PbS[50], Si_xGe_{1-x}[51] and GaN[52], and perovskite materials such as $BaTiO_3$ show phase transitions due to this tension.[53] Applied compressive strain, on the other hand, has been shown to convert $CsPbI_3$ into a metallic ordered phase.[54]

To demonstrate the correlation between the QD size and lattice strain, as well as crystal phase, we performed wide angle X-ray diffraction (XRD) measurements for the $CsPbI_3$ QDs with different sizes. The room temperature structural phase of $CsPbX_3$ has been somewhat in question.[13,55,56] $CsPbI_3$ can exist in three distinct "black" perovskite phases (α, β and γ phases), all with corner sharing octahedra but with subtle differences in degree of symmetry. These three phases have different symmetries with varied distortion of bond angles and the corresponding structure models for all three phases are shown in Figure 2a-c, respectively. The Figure S2 also

Pursuant to the DOE Public Access Plan, this document represents the authors' peer-reviewed, accepted manuscript.
The published version of the article is available from the relevant publisher.

shows the 3D versions of structure models at different angles for each phase. The α phase is cubic, comprised of, on average, undistorted corner sharing lead iodide octahedra. The β phase is a tetragonal distortion of the α phase. In the β phase, the corner sharing lead iodide octahedra rotate and break the cubic symmetry. For the γ phase, there is a second distortion resulting in an orthorhombic structure with an additional tilt of the lead iodide octahedra, further breaking symmetry and doubling the unit cell.

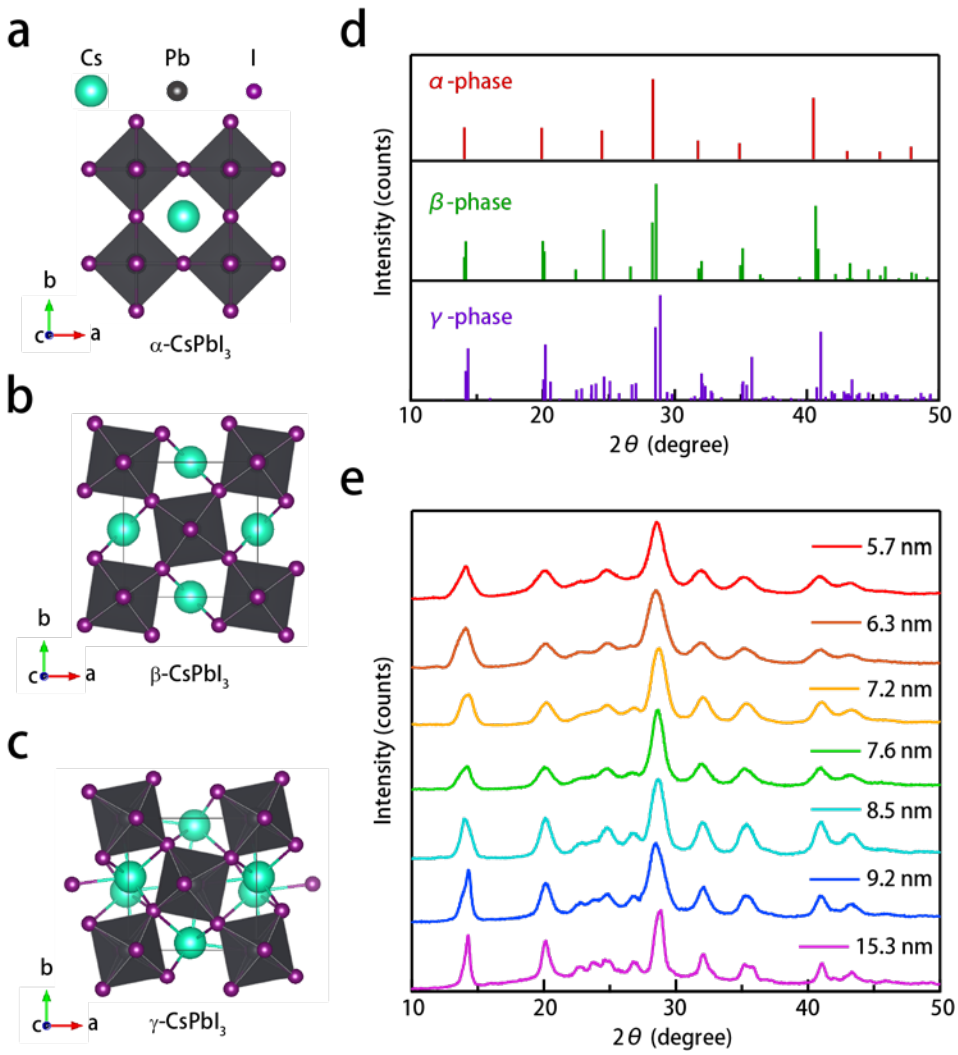

Figure 2. (a-c) Crystal structure model of three perovskite phases with corner-sharing octahedra for $CsPbI_3$ QDs. (d) XRD standard powder patterns for α, β and γ phases plotted with vertical lines corresponding to the diffraction peaks. (e) XRD patterns of $CsPbI_3$ QDs with size 5.7 nm, 6.3 nm, 7.2 nm, 7.6 nm 8.5 nm, 9.2 nm and 15.3 nm.

As shown in Figure 2d, the number of features present in the diffraction pattern increase

Pursuant to the DOE Public Access Plan, this document represents the authors' peer-reviewed, accepted manuscript.
The published version of the article is available from the relevant publisher.

with disorder (from α to β to γ phase).[57] Experimentally, we observed varying distinguishing features in the XRD patterns as a function of the QD size presented in Figure 2e. All $CsPbI_3$ QDs show the characteristic peaks as expected for the α phase perovskite structure. As the NCs increase in size, it becomes easier to resolve the additional peaks between 20 and 28° 2θ, indicting a lower symmetry structure than the cubic-α phase. These peaks are broader and much weaker in the smaller NCs, likely a result of nanoscale broadening or a slight variation in the phase present.

To further understand the size-dependent variations observed in the scattering, we employ Rietveld refinement of the XRD patterns. A representative refinement to the α, β and γ phases for large (15.3 nm) and small (5.7 nm) QDs is shown in Figure 3a–b. For the small $CsPbI_3$ QDs (Figure 3a), the α phase at first glance appears to appropriately capture the structure. However, upon closer inspection, a broad peak observed at 23° 2θ, which indicates lower symmetry than the cubic phase, better describes the sample by either the β or γ phase. However, given the broad nature of the peaks and low intensity, it is difficult to accurately distinguish between these two phases for this size. For larger $CsPbI_3$ QDs (Figure 3b), the γ phase clearly better matches the observed data and the goodnesss of fit (R_{wp}) is significantly better than for the cubic phase (Table S3). This is consistent with other recent literature.[56,58,59] The detailed refinement parameters are presented in the Table S3.

Pursuant to the DOE Public Access Plan, this document represents the authors' peer-reviewed, accepted manuscript.
The published version of the article is available from the relevant publisher.

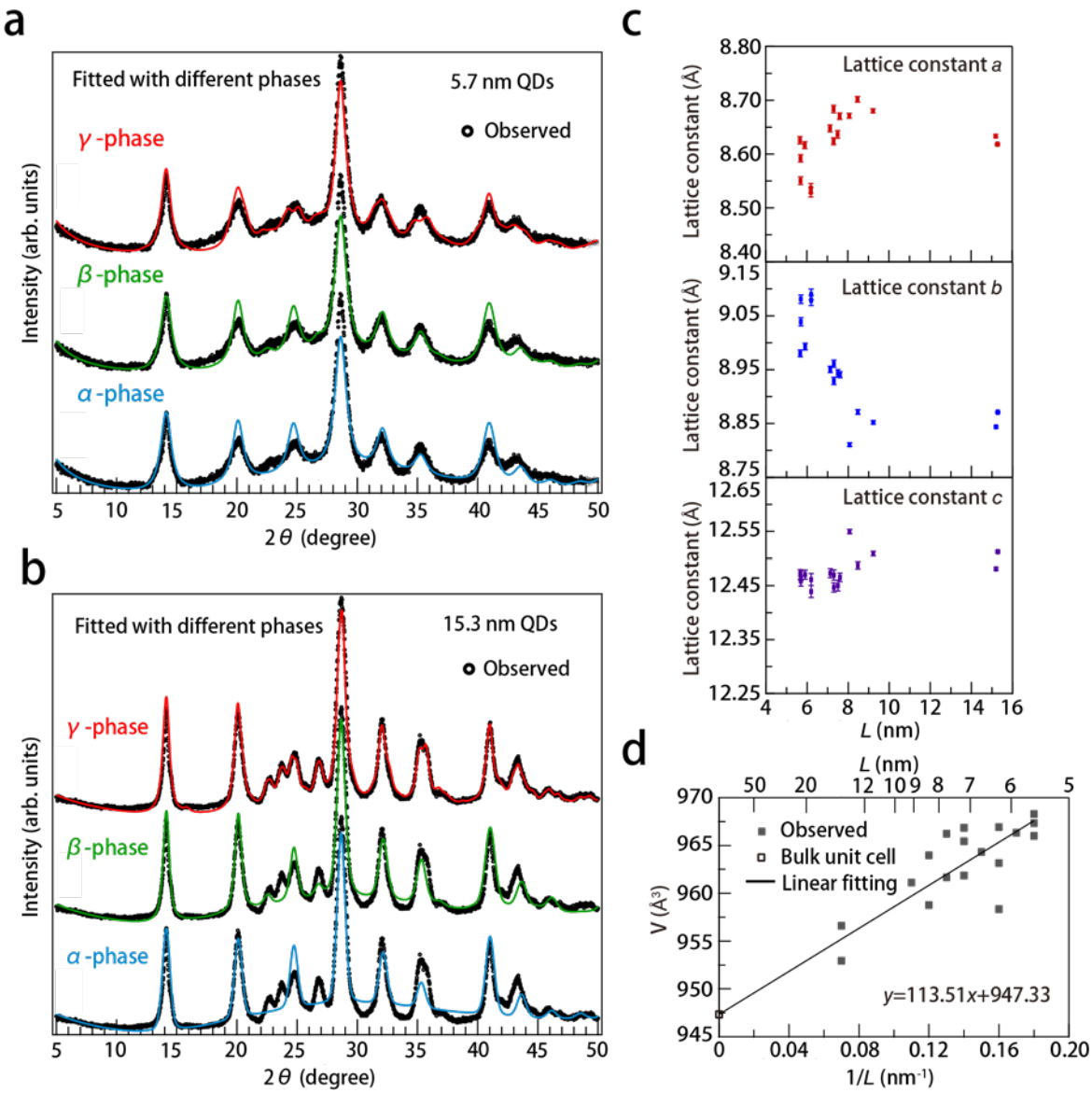

Figure 3. (a and b) Observed (circles) and refined (thin line) XRD profiles of QDs with 5.7 nm (a) and 15.3 nm (b). Rietveld refinements are shown for α, β and γ phases (red, green blue, respectively). (c) Lattice parameters with corresponding error bars of $CsPbI_3$ QDs for various crystal sizes (L) calculated from the refinement using the γ phase. The space groups and initial structures used in the refinements for all phases are extracted from the work of Marronnier et. al[57] and were subsequently refined to best fit the data set. (d) Unit cell volume, $V=a\ b\ c$, plotted versus $1/L$. The values calculated for each sample (solid squares) are fitted to a linear function (solid line). The bulk unit cell volume (hollow square) is taken from the reported by Sutton et al.[55]

To explore the size dependent structure, we plot lattice parameters for all the $CsPbI_3$ QD samples when refined to the γ phase (shown in Figure 3c). Tabulated values can be found in Table S4. As a function of QD size, a clear trend toward smaller lattice parameter is seen for b as the QDs edge length is increased. There is an opposing effect seen in lattice parameter a although it is

Pursuant to the DOE Public Access Plan, this document represents the authors' peer-reviewed, accepted manuscript.
The published version of the article is available from the relevant publisher.

harder to conclude based on the largest samples. One would expect this anticorrelation between various lattice constants based on conventional strain dynamics, for example, in epitaxial systems.[60] The noticeable decrease in lattice parameter *b* shows a trend toward a bulk value[55] (8.86 Å) as size increases, which also suggests an increased average octahedral tilt as a function of QD size. We see very minor variation for lattice parameter *c*. This behavior of the orthorhombic distortion may suggest that the QDs have a larger average octahedral tilting with increasing size; however, in this analysis the lattice parameters are correlated. Despite this uncertainty, the NCs are always best characterized by the γ phase. This leads us to hypothesize that there is a significant size dependent strain present in the NCs which enables the retention of the perovskite structure.[52] To demonstrate this, we plot the unit cell volume ($V = a\ b\ c$) versus $1/L$ in Figure 3e, which clearly shows lattice expansion scaling linearly with $1/L$, consistent with lattice expansion due to negative surface tension[49–52] for our oleate and oleylammonium capped NCs. In the Supporting Information, we analyze the size dependent volume dilatation plotted with $1/L$ in Figure S3 and calculate the surface energy. From these calculations we estimate the surface energy for the ligand stabilized NCs as between -3.0 to -5.1 eV nm^{-2} (~ -1.2 to -2.0 eV per surface unit cell) depending on which estimate is used for the bulk modulus[61,62] and the approximations made in calculating the lattice strain due to surface tension in non-spherical NCs[63,64]. This detailed calculation is discussed in the Supporting Information and the results are summarized in Table S5. This size-dependent tensile strain can have profound effects on the optical properties and has been reported in other systems;[50–52] however, the size dependence of the optical transition energies has not been reported for many perovskite QDs.

To further examine the size dependent properties of $CsPbI_3$ perovskite QDs, we constructed a plot of the exciton energy versus QD size. From this, we then fit models to the data using the strong, weak and intermediate confinement regimes. In the strong confinement regime, valid when NC edge length (L) is much smaller than the exciton radius of the material ($L \ll a_x$), correlation of the electron-hole motion can be neglected and the exciton energy scales as the inverse square of the NC size ($1/L^2$). For cube shaped NCs in this regime, the exciton energy (E_x) is determined by the exciton reduced mass (μ) as Eq. 2, where $1/\mu = 1/m_e + 1/m_h$,

$$E_x = E_g + \frac{\hbar^2}{2\mu}\frac{3\pi^2}{L^2} - 3.05\frac{e^2}{\epsilon L} \quad (2)$$

In Eq. 2, E_g is the bulk bandgap, the second term on the right-hand side represents the kinetic energy of the electron and hole while the third term is the energy of their Coulomb attraction.[65] In

Pursuant to the DOE Public Access Plan, this document represents the authors' peer-reviewed, accepted manuscript.
The published version of the article is available from the relevant publisher.

contrast to the strong confinement regime, the opposite limit is the weak confinement, when L is much larger than a_x ($L >> a_x$). In this weak confinement regime, electron and hole motion is strongly correlated and the exciton exhibits quantum confinement as a whole. The confinement energy scales primarily as $1/L^2$ so that E_x is determined in the weak confinement regime in cube shaped NCs by Eq. 3,

$$E_x = E_g + \frac{\hbar^2}{2M}\frac{3\pi^2}{L^2} - B_x \quad (3)$$

Where B_x is the exciton binding energy. As before, the first term on the right-hand side in Eq. 3 is the bulk bandgap; the second term represents the kinetic energy of the exciton determined by the total exciton mass (M), where $M = m_e + m_h$, while the third term is the exciton binding energy associated with the relative motion of the electron and hole.

Between these two confinement regimes described above, the confinement effects on the electron and hole energies are significant but the motions of the electron and hole are correlated to such a degree that the strong confinement treatment of the Coulomb binding of the electron and hole is inadequate. The energy in this "intermediate" confinement regime[38,65,66] is determined variationally as described in the Supporting Information and bridges between the strong and the weak confinement limits. This model more accurately describes the size dependent properties of perovskite nanocrystals compared to previous published strong confinement models (see Supporting Information discussion). A very good approximation to the exciton energy in this regime is given by Eq. 4,

$$E_x = E_g + \frac{\hbar^2}{2\mu}\frac{3\pi^2}{L^2} - B_x\sqrt{1 + [2 \times 3.047\left(\frac{a_x}{L}\right)]^2} \quad (4)$$

where the first two terms are the same as Eq. 2, and the third term is an approximation to the Coulomb correction in the intermediate confinement regime.

The appropriate confinement model is generally determined by comparing the NC size with the Bohr radius of the exciton. As shown in Figure S4, the calculated exciton energy relative to the bulk bandgap ($E_x - E_g$) is plotted in units of the exciton binding energy (B_x) versus L/a_x. From the plots, it is clear that the energy calculated using the intermediate confinement wavefunction (see Eq. S20 and the description in the Supporting Information) converges to the strong confinement result when L is smaller than about $2a_x$, while it converges to the weak confinement limit when L is larger than about $7a_x$.

Pursuant to the DOE Public Access Plan, this document represents the authors' peer-reviewed, accepted manuscript.
The published version of the article is available from the relevant publisher.

Inspection of Figure S4 makes it clear that when L is larger than $3a_x$, the strong confinement model fails to accurately capture the Coulomb binding of the exciton, which drives the exciton energy below the bulk bandgap. Since perovskite NCs have exciton radius in the 3-4 nm size range,[29] this necessitates use of an intermediate confinement model for perovskite NCs for L larger than about 9 nm. More information on the functional form of the different confinement regimes is presented in the Supporting Information.

We compared the measured size dependent exciton energies with sizing curves calculated applying the strong, weak and intermediate quantum confinement models in an idealized parabolic band system (Figure 4 a and b). The exciton energies of the NCs are determined from the first exciton peak positions in the absorption spectra while the sizes are measured from TEM images as described above. In our calculations we first use the dielectric constant (ϵ_{eff}) and μ determined from exciton magneto-transmission measurements on bulk α-phase $CsPbI_3$ reported by Yang and co-workers[67] due to the lack of reported values for γ phase. Since the measured NC data are taken at 300K, the exciton reduced effective mass is determined using the measured 300K bulk α-phase $CsPbI_3$ bandgap and the Kane energy parameter (E_p) extracted from a 2-band fit to the low temperature bulk reduced mass measured in the literature[67], using Eq. 5.

$$E_p = \frac{3}{2}\frac{E_g}{\mu} \quad (5)$$

Table 1 Summary of electronic structure parameters. For bulk α-phase values of $CsPbI_3$, the experimental parameters for α-phase $CsPbI_3$ NCs are from Yang and co-workers with adjustments for temperature of 300K.[67] The best-fit values are determined by fitting to the $CsPbI_3$ absorption data as shown in Figure 5.

Parameter	α-phase value[66]	The best-fit value
Bandgap E_g	1.805 eV	1.840 eV
Kane energy E_p	22.62 eV	17.39 eV
Exciton reduced mass μ	0.12	0.16
Dielectric constant ϵ_{eff}	10	10 (Constrained)
Exciton radius a_x	4.4 nm	3.3 nm
Exciton binding energy B_x	16.3 meV	21.2 meV

Pursuant to the DOE Public Access Plan, this document represents the authors' peer-reviewed, accepted manuscript.
The published version of the article is available from the relevant publisher.

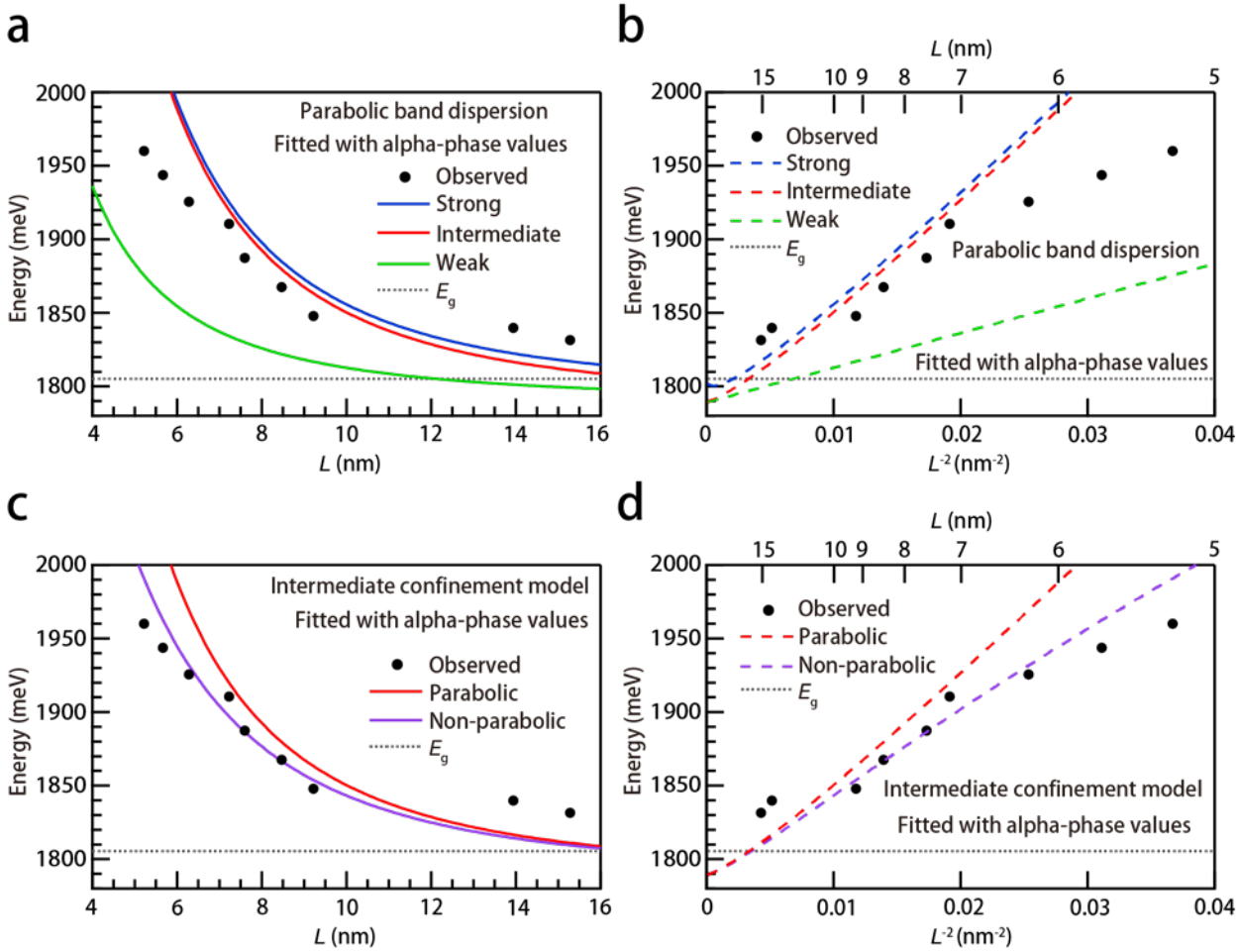

Figure 4. (a and b) Measured vs calculated sizing curves with model calculations in the strong, intermediate and weak confinement approximations, assuming parabolic band dispersion, presented with the blue, red and green lines, respectively. (c and d) Measured *vs.* calculated sizing curves with model calculations with parabolic and non-parabolic approximation in the intermediate confinement regime are shown with the red and purple lines, respectively. Measured 300K data are shown as solid circles. The calculated lines were draw in two ways, $CsPbI_3$ NC absorption peak energy versus NC size L (solid line in a and c) and the absorption peak energy plotted versus the inverse square of NC size $1/L^2$ (dashed line in b and d) that better illustrates the linearity of energy plotted versus $1/L^2$ (see Eq. 2). All model calculations are processed using parameters from the bulk α phase[54] shown in Table 1.

In Figure 4a and b, we show the comparison of the measured NC absorption peak energies against the strong confinement model (blue line), as well as the intermediate confinement model (red line), and the weak confinement model (green line). The weak confinement calculation completely fails to describe the measured data, which is unsurprising since the NCs measured are in a size range outside the range of validity of the weak confinement approximation. The intermediate confinement fit line describes the experimental data slightly better than the strong

Pursuant to the DOE Public Access Plan, this document represents the authors' peer-reviewed, accepted manuscript.
The published version of the article is available from the relevant publisher.

confinement line. However, it is clear in Figure 4a and b that the parabolic band approximation both within the strong and the intermediate confinement models leads to a large overestimation of the exciton energy for small-sized NCs. Both models also undershoot the energy for NCs with L larger than 12 nm.

To address this overestimation of the energy for small-sized NCs, we extend the intermediate confinement model to include band non-parabolicity effects, taking account of conduction-to-valence band coupling in the context of the Kang-Wise NC model.[68] Band non-parabolicity leads to larger effective mass for smaller-sized NCs, reducing the quantum confinement energy relative to that calculated in a parabolic band model. We determined energy dependent effective masses by fitting to a Kang-Wise model calculated with the α-phase parameters in Table 1 for spherical NCs of radius $a_{\text{eff}} = L / \sqrt{3}$. This transformation from L to a_{eff} is exact for the quantum confinement energy of small NCs where non-parabolicity effects are important and where the strong and the intermediate confinement approximations converge. The result is that the exciton reduced mass μ is replaced by a non-parabolic reduced mass ($\mu = m'/2$, where m' is the carrier non-parabolic mass which can be expressed as a function of L as Eq. 6.

$$\frac{m'}{m_0} = \frac{3\left[\sqrt{E_g^2 + \frac{2E_p}{m_0}\hbar^2\left(\frac{\pi}{L}\right)^2} + \sqrt{E_g^2 + \frac{4E_p}{m_0}\hbar^2\left(\frac{\pi}{L}\right)^2}\right]}{2E_p} \quad (6)$$

In this equation, E_p is the Kane energy, m_0 is the free electron mass, and E_g is the bulk bandgap. In Figure 4c and d, we compared the parabolic approximation with the non-parabolic model within the intermediate confinement regime where the exciton energy is plotted versus L and versus $1/L^2$, respectively. With the non-parabolicity corrections, the model calculations approach the measured data more closely in the small-sized range (L < 10nm) as expected, but still fails to describe the measured data in large-sized NCs. This is consistent with the interpretation of the XRD results shown in Figure 3 that the α phase cannot describe the larger NCs.

Pursuant to the DOE Public Access Plan, this document represents the authors' peer-reviewed, accepted manuscript.
The published version of the article is available from the relevant publisher.

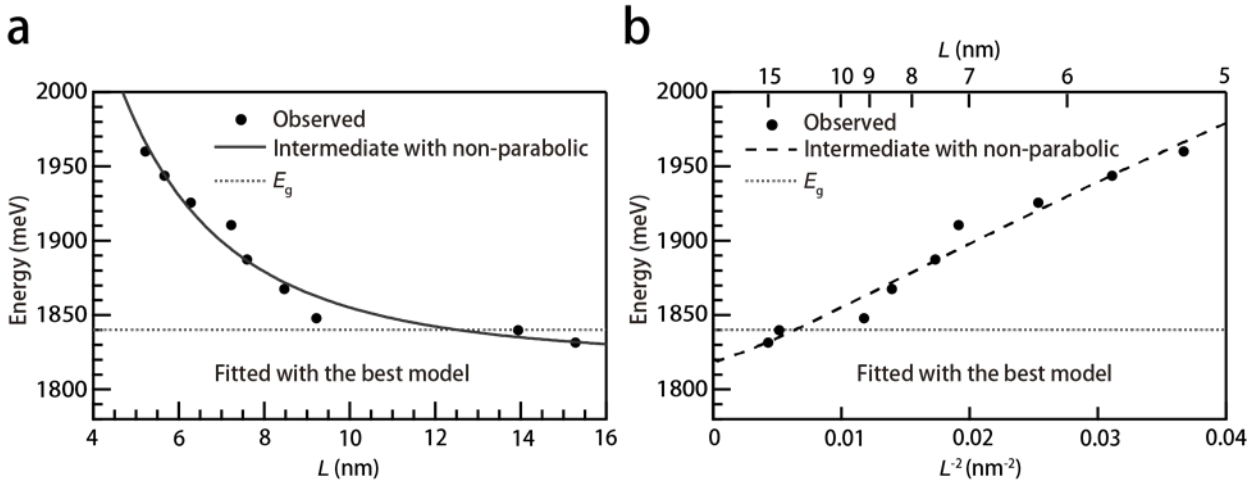

Figure 5. (a and b) Measured vs calculated sizing curves fitted with the best model. The measured absorption peak energies are plotted versus L (a) and $1/L^2$ (b), respectively. Measured 300K data are shown as solid circle points in the figures. The theoretical curves shown are calculated using the intermediate confinement model with band non-parabolicity effects.

Therefore, based on the intermediate confinement models with non-parabolic corrections that was developed with the bulk α-phase values, we adjust the electronic structure parameters presented in Table 1 to build the best-fit model to match our measured data. From Figure 5, we observe that our best-fit model yields a good fit to the measured data, resulting in modified electronic structure parameters shown in Table 1. Notably, the modified bandgap is larger than the bulk α-phase bandgap by 35 meV and the exciton reduced effective mass is larger than the bulk α-phase value by 33%, consistent with theoretical expectations of slightly increased bandgap and heavier effective masses in γ phase versus α phase.[69] This study not only allows us to confirm that the $CsPbI_3$ QDs are clearly not in the α phase, but also provides more accurate electronic structure parameters for γ-$CsPbI_3$ in general. Therefore, materials parameters for MHPs in various distorted phases are understudied and should be further explored. Additionally, we also show results of a similar calculation performed on $CsPbBr_3$ NCs as a check on the developed methods in the Supporting Information. There it is shown in Figure S5 that the non-parabolic intermediate confinement model can also be applied to achieve a good fit to the published $CsPbBr_3$ NC absorption data[42] using the measured bulk γ-phase parameters[68] shown in Table S6.

Given the changing lattice parameters as a function of size with smaller nanocrystals experiencing greater tensile strain, we calculated how much this additional effect may change the sizing curve analysis in the intermediate confinement regime. First, we determined the unit cell volume dilatation as a function of nanocrystal size from the lattice constant data in Figure 3c.

Pursuant to the DOE Public Access Plan, this document represents the authors' peer-reviewed, accepted manuscript.
The published version of the article is available from the relevant publisher.

Calculating the corresponding change in bandgap using Eq. S22, we performed a linear interpolation shown in Eq. S25 and Figure S6. This strain would cause the optical transition energy to increase in the same direction as quantum-confinement-induced changes, however only by a very small (~5 meV), almost insignificant, amount. The sizing curve accounting for this additional component is shown in Figure S7; inclusion of strain effects causes a negligible change in some material constants such as tabulated in Table S7.

Conclusions

$CsPbI_3$ perovskite QDs with relatively narrow size distribution and controllable size within 5-15 nm range enable us to appropriately characterize the size dependent optical and structural properties. $CsPbI_3$ NCs show a size-dependent lattice structure best represented by the γ phase rather than the α phase. $CsPbI_3$ QDs in this size range show pronounced quantum confinement effects including sharp excitonic emission and absorption peaks exhibiting confinement related blue shifts with decreasing size. Furthermore, the size dependent excitons of the samples are best described by an intermediate confinement model with non-parabolic bands and revised electronic structure parameters compared to known parameters for high temperature cubic phase α-$CsPbI_3$. We envision that detailed studies such as this with perovskite NCs as model systems will enable the research community to better understand the stabilization of the perovskite phase of $CsPbI_3$ in thin film or in bulk using strain engineering.

Methods:

Materials. Oleylamine (OAm; technical grade, 70%), 1-octadecene (ODE; technical grade, 90%), Cesium carbonate (Cs_2CO_3; 99.9%), oleic acid (OA; technical grade, 90%), methyl acetate (MeOAc; anhydrous, 99.5%), octane (anhydrous, ≥99%), lead nitrate ($Pb(NO_3)_2$; 99.999%), hexane (reagent grade, ≥95%), formamidinium acetate (FA-acetate, 99%) were purchased from Sigma-Aldrich and used as received unless otherwise specified.

$CsPbI_3$ QD synthesis. The synthesis was performed following the method reported in our previous publications with slight modification.[70,71] First, 20 mL of ODE is mixed with 1.25 mL of OA containing 0.407 g of Cs_2CO_3. This was degassed at 120°C for 20 min under vacuum in a three-neck flask to form Cs-oleate. The Cs-oleate precursor was kept under N_2 instead of vacuum after Cs_2CO_3 was completely dissolved in the solution. Then the PbI_2 precursor was formed by mixing 0.5 g of PbI_2 and 25 mL of ODE in a three-neck flask and heated at 120°C for 20 min under vacuum. A preheated mixture of OA and OAm (135°C, 2.5 mL each) was transferred into the PbI_2 solution that was kept at 120°C under vacuum. After the PbI_2 completely dissolved in the solution, the reaction flask was heated to the desired temperature (140, 160, or 180°C) under flowing N_2.

Pursuant to the DOE Public Access Plan, this document represents the authors' peer-reviewed, accepted manuscript.
The published version of the article is available from the relevant publisher.

Then 2 mL of the Cs-oleate precursor was swiftly injected into the reaction flask. In general, smaller nanocrystals are obtained with lower growth and larger are obtained with higher temperature, but some sizes overlap this trend when using the size selective precipitation. Immediately after the reaction, the mixture was quenched by submerging the flask into an ice bath within 3 s after the injection. After cooling to room temperature, 70 mL of MeOAc was added into the colloidal solution and the mixed solution was centrifuged at 7500 rpm for 5 min. The precipitated $CsPbI_3$ QDs was dispersed in 10 mL of hexane.

$CsPbI_3$ QDs size-selective precipitation and purification. MeOAc was added in the initial $CsPbI_3$ QD solution in a volume ratio of 1 : 3. After centrifugation at 7500 rpm for 5 min, larger NCs were precipitated. The supernatant was decanted and MeOAc was added to it in a volume ratio of 1 : 3 and the mixed solution was centrifuged at 7500 rpm for 5 min, producing another batch of precipitates. This process was repeated multiple times until there is no obvious precipitation of QDs from the supernatant. The resulting precipitate from every batch was redispersed in 3 mL of hexane. The obtained QD solution was centrifuged at 7500 rpm for 5 min and the precipitate was decarded. The supernatant was filtered through a 0.45 μm nylon filter and then kept in a sealed vial for characterization.

$CsPbI_3$ QDs Characterization. TEM images were obtained using a FEI Tecnai F20 electron microscope with 200 kV accelerating voltage. Ultraviolet-visible absorption spectra were measured using a Shimadzu UV-3600 UV-vis-NIR spectrophotometer. Steady-state photoluminescence (PL) spectra were recorded with a 450 nm excitation by a Horiba Jobin Yvon fluoromax-4 spectrophotometer. Powder X-ray diffraction (XRD) data were obtained using a Rigaku's DMax diffractometer with Cu-kα radiation (wavelength 1.5406 Å) operated at 40 kV and 250 mA, with a step width of 0.02° and a count time of 1.0 s in the 2θ range from 3° to 70°. Reference markers for XRD are calculated with Mercury software employing the reported crystallographic information[56].The Rietveld refinement of the XRD data was performed using the TOPAS-Academic software package.

Acknowledgements:
This work (QD synthesis, size dependent analysis) was supported by the Center for Hybrid Organic Inorganic Semiconductors for Energy (CHOISE), an Energy Frontier Research Center funded by the Office of Science, Office of Basic Energy Sciences within the U.S. Department of Energy. This work was authored in part by the Alliance for Sustainable Energy, Limited Liability Company, the manager and operator of the National Renewable Energy Laboratory under Contract No. DE-AC36-08GO28308. The views expressed in the article do not necessarily represent the views of the Department of Energy or the U.S. Government. Q.Z. acknowledges fellowship support from the China Scholarship Council, Natural Science Foundation of Tianjin (18JCZDJC31000) and Natural Science of Foundation China (21576140). L.T.S. was supported by the U.S. Department of Energy (DOE) Solar Energy Technology Office (SETO) of the Energy Efficiency and Renewable Energy (EERE) award for the De-risking Halide Perovskite Solar Cells project. The authors thank Matthew C. Beard, Ashley R. Marshall, Jeffrey A. Christians and Erin M. Sanehira for helpful discussion.

Data Availability:

Pursuant to the DOE Public Access Plan, this document represents the authors' peer-reviewed, accepted manuscript.
The published version of the article is available from the relevant publisher.

Data that support the plots within this work are available from the corresponding author upon reasonable request.

Competing Interests:
The authors declare no competing financial interests.

References:

(1) Bai, S.; Da, P.; Li, C.; Wang, Z.; Yuan, Z.; Fu, F.; Kawecki, M.; Liu, X.; Sakai, N.; Wang, J. T.-W.; et al. Planar Perovskite Solar Cells with Long-Term Stability Using Ionic Liquid Additives. *Nature* **2019**, *571*, 245–250.

(2) Wei, H.; Huang, J. Halide Lead Perovskites for Ionizing Radiation Detection. *Nat. Commun.* **2019**, *10*, 1066.

(3) Chen, Q.; Wu, J.; Ou, X.; Huang, B.; Almutlaq, J.; Zhumekenov, A. A.; Guan, X.; Han, S.; Liang, L.; Yi, Z.; et al. All-Inorganic Perovskite Nanocrystal Scintillators. *Nature* **2018**, *561*, 88–93.

(4) Jiang, Y.; Qin, C.; Cui, M.; He, T.; Liu, K.; Huang, Y.; Luo, M.; Zhang, L.; Xu, H.; Li, S.; et al. Spectra Stable Blue Perovskite Light-Emitting Diodes. *Nat. Commun.* **2019**, *10*, 1868.

(5) Akkerman, Q. A.; Rainò, G.; Kovalenko, M. V; Manna, L. Genesis, Challenges and Opportunities for Colloidal Lead Halide Perovskite Nanocrystals. *Nat. Mater.* **2018**, *17*, 394–405.

(6) Christians, J. A.; Habisreutinger, S. N.; Berry, J. J.; Luther, J. M. Stability in Perovskite Photovoltaics: A Paradigm for Newfangled Technologies. *ACS Energy Lett.* **2018**, *3*, 2136–2143.

(7) Govinda, S.; Kore, B. P.; Bokdam, M.; Mahale, P.; Kumar, A.; Pal, S.; Bhattacharyya, B.; Lahnsteiner, J.; Kresse, G.; Franchini, C.; et al. Behavior of Methylammonium Dipoles in $MAPbX_3$ (X = Br and I). *J. Phys. Chem. Lett.* **2017**, *8*, 4113–4121.

(8) Seol, D.; Han, G. S.; Bae, C.; Shin, H.; Jung, H. S.; Kim, Y. Screening Effect on Photovoltaic Performance in Ferroelectric CH3NH3PbI3 Perovskite Thin Films. *J. Mater. Chem. A* **2015**, *3*, 20352–20358.

(9) Sun, J. K.; Huang, S.; Liu, X. Z.; Xu, Q.; Zhang, Q. H.; Jiang, W. J.; Xue, D. J.; Xu, J. C.; Ma, J.-Y.; Ding, J.; et al. Polar Solvent Induced Lattice Distortion of Cubic $CsPbI_3$ Nanocubes and Hierarchical Self-Assembly into Orthorhombic Single-Crystalline Nanowires. *J. Am. Chem. Soc.* **2018**, *140*, 11705–11715.

(10) Wu, T.; Wang, Y.; Dai, Z.; Cui, D.; Wang, T.; Meng, X.; Bi, E.; Yang, X.; Han, L. Efficient and Stable $CsPbI_3$ Solar Cells via Regulating Lattice Distortion with Surface Organic Terminal Groups. *Adv. Mater.* **2019**, *31*, 1900605.

(11) Herz, L. M. How Lattice Dynamics Moderate the Electronic Properties of Metal-Halide Perovskites. *J. Phys. Chem. Lett.* **2018**, *9*, 6853–6863.

(12) Zhao, Q.; Hazarika, A.; Chen, X.; Harvey, S. P.; Larson, B. W.; Teeter, G. R.; Liu, J.; Song, T.; Xiao, C.; Shaw, L.; et al. High Efficiency Perovskite Quantum Dot Solar Cells with Charge Separating Heterostructure. *Nat. Commun.* **2019**, *10*, 2842.

(13) Swarnkar, A.; Marshall, A. R.; Sanehira, E. M.; Chernomordik, B. D.; Moore, D. T.; Christians, J. A.; Chakrabarti, T.; Luther, J. M. Quantum Dot–induced Phase Stabilization of α-$CsPbI_3$ Perovskite for High-Efficiency Photovoltaics. *Science.* **2016**, *354*, 92–95.

(14) Zou, C.; Huang, C. Y.; Sanehira, E. M.; Luther, J. M.; Lin, L. Y. Highly Stable Cesium Lead Iodide Perovskite Quantum Dot Light-Emitting Diodes. *Nanotechnology* **2017**, *28*,

Pursuant to the DOE Public Access Plan, this document represents the authors' peer-reviewed, accepted manuscript.
The published version of the article is available from the relevant publisher.

455201.
(15) Ling, X.; Zhou, S.; Yuan, J.; Shi, J.; Qian, Y.; Larson, B. W.; Zhao, Q.; Qin, C.; Li, F.; Shi, G.; et al. 14.1% $CsPbI_3$ Perovskite Quantum Dot Solar Cells via Cesium Cation Passivation. *Adv. Energy Mater.* **2019**, *9*, 1900721.
(16) Gaulding, E. A.; Hao, J.; Kang, H. S.; Miller, E. M.; Habisreutinger, S. N.; Zhao, Q.; Hazarika, A.; Sercel, P. C.; Luther, J. M.; Blackburn, J. L. Conductivity Tuning via Doping with Electron Donating and Withdrawing Molecules in Perovskite $CsPbI_3$ Nanocrystal Films. *Adv. Mater.* **2019**, *31*, 1902250.
(17) Liu, F.; Ding, C.; Zhang, Y.; Kamisaka, T.; Zhao, Q.; Luther, J. M.; Toyoda, T.; Hayase, S.; Minemoto, T.; Yoshino, K.; et al. GeI_2 Additive for High Optoelectronic Quality $CsPbI_3$ Quantum Dots and Their Application in Photovoltaic Devices. *Chem. Mater.* **2019**, *31*, 798–807.
(18) Wang, Q.; Jin, Z.; Chen, D.; Bai, D.; Bian, H.; Sun, J.; Zhu, G.; Wang, G.; Liu, S. (Frank). μ-Graphene Crosslinked $CsPbI_3$ Quantum Dots for High Efficiency Solar Cells with Much Improved Stability. *Adv. Energy Mater.* **2018**, *8*, 1800007.
(19) Ferreira, A. C.; Létoublon, A.; Paofai, S.; Raymond, S.; Ecolivet, C.; Rufflé, B.; Cordier, S.; Katan, C.; Saidaminov, M. I.; Zhumekenov, A. A.; et al. Elastic Softness of Hybrid Lead Halide Perovskites. *Phys. Rev. Lett.* **2018**, *121*, 85502.
(20) Miyata, K.; Atallah, T. L.; Zhu, X.-Y. Lead Halide Perovskites: Crystal-Liquid Duality, Phonon Glass Electron Crystals, and Large Polaron Formation. *Sci. Adv.* **2017**, *3*, e1701469.
(21) Quarti, C.; Mosconi, E.; Ball, J. M.; D'Innocenzo, V.; Tao, C.; Pathak, S.; Snaith, H. J.; Petrozza, A.; De Angelis, F. Structural and Optical Properties of Methylammonium Lead Iodide across the Tetragonal to Cubic Phase Transition: Implications for Perovskite Solar Cells. *Energy Environ. Sci.* **2016**, *9*, 155–163.
(22) Steele, J. A.; Jin, H.; Dovgaliuk, I.; Berger, R. F.; Braeckevelt, T.; Yuan, H.; Martin, C.; Solano, E.; Lejaeghere, K.; Rogge, S. M. J.; et al. Thermal Unequilibrium of Strained Black $CsPbI_3$ Thin Films. *Science* **2019**, *365*, 679–684.
(23) Ghosh, D.; Aziz, A.; Dawson, J. A.; Walker, A. B.; Islam, M. S. Putting the Squeeze on Lead Iodide Perovskites: Pressure-Induced Effects To Tune Their Structural and Optoelectronic Behavior. *Chem. Mater.* **2019**, *31*, 4063–4071.
(24) Liu, M.; Chen, Y.; Tan, C.-S.; Quintero-Bermudez, R.; Proppe, A. H.; Munir, R.; Tan, H.; Voznyy, O.; Scheffel, B.; Walters, G.; et al. Lattice Anchoring Stabilizes Solution-Processed Semiconductors. *Nature* **2019**, *570*, 96–101.
(25) Klarbring, J.; Simak, S. I. Nature of the Octahedral Tilting Phase Transitions in Perovskites: A Case Study of $CaMnO_3$. *Phys. Rev. B* **2018**, *97*, 24108.
(26) Frost, J. M.; Butler, K. T.; Brivio, F.; Hendon, C. H.; van Schilfgaarde, M.; Walsh, A. Atomistic Origins of High-Performance in Hybrid Halide Perovskite Solar Cells. *Nano Lett.* **2014**, *14*, 2584–2590.
(27) Zhou, Y.; You, L.; Wang, S.; Ku, Z.; Fan, H.; Schmidt, D.; Rusydi, A.; Chang, L.; Wang, L.; Ren, P.; et al. Giant Photostriction in Organic–inorganic Lead Halide Perovskites. *Nat. Commun.* **2016**, *7*, 11193.
(28) Chen, B.; Li, T.; Dong, Q.; Mosconi, E.; Song, J.; Chen, Z.; Deng, Y.; Liu, Y.; Ducharme, S.; Gruverman, A.; et al. Large Electrostrictive Response in Lead Halide Perovskites. *Nat. Mater.* **2018**, *17*, 1020–1026.
(29) Protesescu, L.; Yakunin, S.; Bodnarchuk, M. I.; Krieg, F.; Caputo, R.; Hendon, C. H.; Yang, R. X.; Walsh, A.; Kovalenko, M. V. Nanocrystals of Cesium Lead Halide Perovskites

Pursuant to the DOE Public Access Plan, this document represents the authors' peer-reviewed, accepted manuscript.
The published version of the article is available from the relevant publisher.

($CsPbX_3$, X = Cl, Br, and I): Novel Optoelectronic Materials Showing Bright Emission with Wide Color Gamut. *Nano Lett.* **2015**, *15*, 3692–3696.
(30) Lignos, I.; Stavrakis, S.; Nedelcu, G.; Protesescu, L.; deMello, A. J.; Kovalenko, M. V. Synthesis of Cesium Lead Halide Perovskite Nanocrystals in a Droplet-Based Microfluidic Platform: Fast Parametric Space Mapping. *Nano Lett.* **2016**, *16*, 1869–1877.
(31) Weidman, M. C.; Beck, M. E.; Hoffman, R. S.; Prins, F.; Tisdale, W. A. Monodisperse, Air-Stable PbS Nanocrystals via Precursor Stoichiometry Control. *ACS Nano* **2014**, *8*, 6363–6371.
(32) de Mello Donegá, C.; Hickey, S. G.; Wuister, S. F.; Vanmaekelbergh, D.; Meijerink, A. Single-Step Synthesis to Control the Photoluminescence Quantum Yield and Size Dispersion of CdSe Nanocrystals. *J. Phys. Chem. B* **2003**, *107*, 489–496.
(33) Ravi, V. K.; Swarnkar, A.; Chakraborty, R.; Nag, A. Excellent Green but Less Impressive Blue Luminescence from $CsPbBr_3$ perovskite Nanocubes and Nanoplatelets. *Nanotechnology* **2016**, *27*, 325708.
(34) Seth, S.; Samanta, A. A Facile Methodology for Engineering the Morphology of $CsPbX_3$ Perovskite Nanocrystals under Ambient Condition. *Sci. Rep.* **2016**, *6*, 37693.
(35) Huang, H.; Susha, A. S.; Kershaw, S. V; Hung, T. F.; Rogach, A. L. Control of Emission Color of High Quantum Yield $CH_3NH_3PbBr_3$ Perovskite Quantum Dots by Precipitation Temperature. *Adv. Sci.* **2015**, *2*, 1500194.
(36) Li, D.; Yun, H.; Diroll, B. T.; Doan-Nguyen, V. V. T.; Kikkawa, J. M.; Murray, C. B. Synthesis and Size-Selective Precipitation of Monodisperse Nonstoichiometric $MxFe_{3-x}O_4$ (M = Mn, Co) Nanocrystals and Their DC and AC Magnetic Properties. *Chem. Mater.* **2016**, *28*, 480–489.
(37) Ferreira, D. L.; Silva, F. O.; Viol, L. C. S.; Schiavon, M. A.; Licinio, P.; Valadares, M.; Cury, L. A.; Alves, J. L. A. Size Selective Precipitation of CdSe Colloidal Quantum Dots. *AIP Conf. Proc.* **2010**, *1199*, 309–310.
(38) Zhang, J.; Gao, J.; Miller, E. M.; Luther, J. M.; Beard, M. C. Diffusion-Controlled Synthesis of PbS and PbSe Quantum Dots with in Situ Halide Passivation for Quantum Dot Solar Cells. *ACS Nano* **2014**, *8*, 614–622.
(39) Dong, Y.; Qiao, T.; Kim, D.; Parobek, D.; Rossi, D.; Son, D. H. Precise Control of Quantum Confinement in Cesium Lead Halide Perovskite Quantum Dots via Thermodynamic Equilibrium. *Nano Lett.* **2018**, *18*, 3716–3722.
(40) Imran, M.; Ijaz, P.; Baranov, D.; Goldoni, L.; Petralanda, U.; Akkerman, Q.; Abdelhady, A. L.; Prato, M.; Bianchini, P.; Infante, I.; et al. Shape-Pure, Nearly Monodispersed $CsPbBr_3$ Nanocubes Prepared Using Secondary Aliphatic Amines. *Nano Lett.* **2018**, *18*, 7822–7831.
(41) Brennan, M. C.; Zinna, J.; Kuno, M. Existence of a Size-Dependent Stokes Shift in $CsPbBr_3$ Perovskite Nanocrystals. *ACS Energy Lett.* **2017**, *2*, 1487–1488.
(42) Brennan, M. C.; Herr, J. E.; Nguyen-Beck, T. S.; Zinna, J.; Draguta, S.; Rouvimov, S.; Parkhill, J.; Kuno, M. Origin of the Size-Dependent Stokes Shift in $CsPbBr_3$ Perovskite Nanocrystals. *J. Am. Chem. Soc.* **2017**, *139*, 12201–12208.
(43) Schelhas, L. T.; Christians, J. A.; Berry, J. J.; Toney, M. F.; Tassone, C. J.; Luther, J. M.; Stone, K. H. Monitoring a Silent Phase Transition in $CH_3NH_3PbI_3$ Solar Cells via Operando X-Ray Diffraction. *ACS Energy Lett.* **2016**, *1*, 1007–1012.
(44) Sutton, R. J.; Eperon, G. E.; Miranda, L.; Parrott, E. S.; Kamino, B. A.; Patel, J. B.; Hörantner, M. T.; Johnston, M. B.; Haghighirad, A. A.; Moore, D. T.; et al. Bandgap-Tunable Cesium Lead Halide Perovskites with High Thermal Stability for Efficient Solar

Pursuant to the DOE Public Access Plan, this document represents the authors' peer-reviewed, accepted manuscript.
The published version of the article is available from the relevant publisher.

Cells. *Adv. Energy Mater.* **2016**, *6*, 1502458.
(45) Sharma, S.; Weiden, N.; Weiss, A.;Phase Diagrams of Quasibinary Systems of the Type: ABX_3—$A'BX_3$; ABX_3—$AB'X_3$, and ABX_3—ABX'_3; X=Halogen. *Zeitschrift für Physikalische Chemie*. 1992, *175*, 63–80.
(46) Han, Q.; Bae, S.-H.; Sun, P.; Hsieh, Y.-T.; Yang, Y. (Michael); Rim, Y. S.; Zhao, H.; Chen, Q.; Shi, W.; Li, G.; et al. Single Crystal Formamidinium Lead Iodide ($FAPbI_3$): Insight into the Structural, Optical, and Electrical Properties. *Adv. Mater.* **2016**, *28*, 2253–2258.
(47) Liu, Y.; Yang, Z.; Cui, D.; Ren, X.; Sun, J.; Liu, X.; Zhang, J.; Wei, Q.; Fan, H.; Yu, F.; et al. Two-Inch-Sized Perovskite $CH_3NH_3PbX_3$ (X = Cl, Br, I) Crystals: Growth and Characterization. *Adv. Mater.* **2015**, *27*, 5176–5183.
(48) Zhang, J.; Hodes, G.; Jin, Z.; Liu, S. All-Inorganic $CsPbX_3$ Perovksite Solar Cells: Progress and Prospects. *Angew. Chemie Int. Ed.* **2019**, DOI: 10.1002/anie.201901081.
(49) Wei, Z.; Xia, T.; Ma, J.; Feng, W.; Dai, J.; Wang, Q.; Yan, P. Investigation of the Lattice Expansion for Ni Nanoparticles. *Mater. Charact.* **2007**, *58*, 1019–1024.
(50) Bertolotti, F.; Dirin, D. N.; Ibań̃ez, M.; Krumeich, F.; Cervellino, A.; Frison, R.; Voznyy, O.; Sargent, E. H.; Kovalenko, M. V.; Guagliardi, A.; Masciocchi, N. Crystal symmetry breaking and vacancies in colloidal lead chalcogenide quantum dots. *Nat. Mater*. **2016**, *15*, 987.
(51) Shreiber, D.; Jesser, W. A. Size Dependence of Lattice Parameter for Si_xGe_{1-x} Nanoparticles. *Surf. Sci.* **2006**, *600*, 4584–4590.
(52) Diehm, P. M.; Ágoston, P.; Albe, K. Size-Dependent Lattice Expansion in Nanoparticles: Reality or Anomaly? *ChemPhysChem* **2012**, *13*, 2443–2454.
(53) Tsunekawa, S.; Ishikawa, K.; Li, Z.-Q.; Kawazoe, Y.; Kasuya, A. Origin of Anomalous Lattice Expansion in Oxide Nanoparticles. *Phys. Rev. Lett.* **2000**, *85*, 3440–3443.
(54) Liang, Y.; Huang, X.; Huang, Y.; Wang, X.; Li, F.; Wang, Y.; Tian, F.; Liu, B.; Shen, Z. X.; Cui, T. New Metallic Ordered Phase of Perovskite $CsPbI_3$ under Pressure. *Adv. Sci.* **2019**, *6*, 1900399.
(55) Sutton, R. J.; Filip, M. R.; Haghighirad, A. A.; Sakai, N.; Wenger, B.; Giustino, F.; Snaith, H. J. Cubic or Orthorhombic? Revealing the Crystal Structure of Metastable Black-Phase $CsPbI_3$ by Theory and Experiment. *ACS Energy Lett.* **2018**, *3*, 1787–1794.
(56) Brennan, M. C.; Kuno, M.; Rouvimov, S. Crystal Structure of Individual $CsPbBr_3$ Perovskite Nanocubes. *Inorg. Chem.* **2019**, *58*, 1555–1560.
(57) Marronnier, A.; Roma, G.; Boyer-Richard, S.; Pedesseau, L.; Jancu, J.-M.; Bonnassieux, Y.; Katan, C.; Stoumpos, C. C.; Kanatzidis, M. G.; Even, J. Anharmonicity and Disorder in the Black Phases of Cesium Lead Iodide Used for Stable Inorganic Perovskite Solar Cells. *ACS Nano* **2018**, *12*, 3477–3486.
(58) Bertolotti, F.; Protesescu, L.; Kovalenko, M. V; Yakunin, S.; Cervellino, A.; Billinge, S. J. L.; Terban, M. W.; Pedersen, J. S.; Masciocchi, N.; Guagliardi, A. Coherent Nanotwins and Dynamic Disorder in Cesium Lead Halide Perovskite Nanocrystals. *ACS Nano* **2017**, *11*, 3819–3831.
(59) Becker, P.; Márquez, J. A.; Just, J.; Al-Ashouri, A.; Hages, C.; Hempel, H.; Jošt, M.; Albrecht, S.; Frahm, R.; Unold, T. Low Temperature Synthesis of Stable γ-CsPbI3 Perovskite Layers for Solar Cells Obtained by High Throughput Experimentation. *Adv. Energy Mater.* **2019**, *9*, 1900555.
(60) Bakti Utama, M. I.; Zhang, Q.; Zhang, J.; Yuan, Y.; Belarre, F. J.; Arbiol, J.; Xiong, Q. Recent Developments and Future Directions in the Growth of Nanostructures by van Der

Pursuant to the DOE Public Access Plan, this document represents the authors' peer-reviewed, accepted manuscript.
The published version of the article is available from the relevant publisher.

Waals Epitaxy. *Nanoscale* **2013**, *5*, 3570–3588.
(61) Jong, U. G.; Yu, C. J.; Kye, Y. H.; Kim, Y. S.; Kim, C. H.; Ri, S. G. A First-Principles Study on the Chemical Stability of Inorganic Perovskite Solid Solutions $Cs_{1-x}Rb_xPbI_3$ at Finite Temperature and Pressure. *J. Mater. Chem. A* **2018**, *6*, 17994–18002.
(62) Rakita, Y.; Cohen, S. R.; Kedem, N. K.; Hodes, G.; Cahen, D. Mechanical Properties of $APbX_3$ (A = Cs or CH_3NH_3; X = I or Br) Perovskite Single Crystals. *MRS Commun.* **2015**, *5*, 623–629.
(63) Weissmüller, J.; Cahn, J. W. Mean Stresses in Microstructures Due to Interface Stresses: A Generalization of a Capillary Equation for Solids. *Acta Mater.* **1997**, *45*, 1899–1906.
(64) Huang, Z.; Thomson, P.; Di, S. Lattice Contractions of a Nanoparticle Due to the Surface Tension: A Model of Elasticity. *J. Phys. Chem. Solids* **2007**, *68*, 530–535.
(65) Sercel, P. C.; Lyons, J. L.; Wickramaratne, D.; Vaxenburg, R.; Bernstein, N.; Efros, A. L. Exciton Fine Structure in Perovskite Nanocrystals. *Nano Lett.* **2019**, *19*, 4068–4077.
(66) Becker, M. A.; Vaxenburg, R.; Nedelcu, G.; Sercel, P. C.; Shabaev, A.; Mehl, M. J.; Michopoulos, J. G.; Lambrakos, S. G.; Bernstein, N.; Lyons, J. L.; et al. Bright Triplet Excitons in Caesium Lead Halide Perovskites. *Nature* **2018**, *553*, 189.
(67) Yang, Z.; Surrente, A.; Galkowski, K.; Miyata, A.; Portugall, O.; Sutton, R. J.; Haghighirad, A. A.; Snaith, H. J.; Maude, D. K.; Plochocka, P.; et al. Impact of the Halide Cage on the Electronic Properties of Fully Inorganic Cesium Lead Halide Perovskites. *ACS Energy Lett.* **2017**, *2*, 1621–1627.
(68) Kang, I.; Wise, F. W. Electronic Structure and Optical Properties of PbS and PbSe Quantum Dots. *J. Opt. Soc. Am. B* **1997**, *14*, 1632–1646.
(69) Amat, A.; Mosconi, E.; Ronca, E.; Quarti, C.; Umari, P.; Nazeeruddin, M. K.; Grätzel, M.; De Angelis, F. Cation-Induced Band-Gap Tuning in Organohalide Perovskites: Interplay of Spin–Orbit Coupling and Octahedra Tilting. *Nano Lett.* **2014**, *14*, 3608–3616.
(70) Hazarika, A.; Zhao, Q.; Gaulding, E. A.; Christians, J. A.; Dou, B.; Marshall, A. R.; Moot, T.; Berry, J. J.; Johnson, J. C.; Luther, J. M. Perovskite Quantum Dot Photovoltaic Materials beyond the Reach of Thin Films: Full-Range Tuning of A-Site Cation Composition. *ACS Nano* **2018**, *12*, 10327–10337.
(71) Wheeler, L. M.; Sanehira, E. M.; Marshall, A. R.; Schulz, P.; Suri, M.; Anderson, N. C.; Christians, J. A.; Nordlund, D.; Sokaras, D.; Kroll, T.; et al. Targeted Ligand-Exchange Chemistry on Cesium Lead Halide Perovskite Quantum Dots for High-Efficiency Photovoltaics. *J. Am. Chem. Soc.* **2018**, *140*, 10504–10513.

Pursuant to the DOE Public Access Plan, this document represents the authors' peer-reviewed, accepted manuscript.
The published version of the article is available from the relevant publisher.